



Coexistence of superparamagnetism and spin-glass like behavior in zinc-substituted cobalt ferrite nanoparticles

Gassem M. Alzoubi¹ · A. M. Alsmadi^{1,2} · G. A. Alna'washi¹ · B. Salameh² · M. Shatnawi¹ · Sufian Alnemrat¹ · B. A. Albiss³ · I. Bsoul⁴

Received: 1 April 2020 / Accepted: 18 May 2020 / Published online: 11 June 2020
© Springer-Verlag GmbH Germany, part of Springer Nature 2020

Abstract

We have performed a systematic study on the effect of Zn substitution on the structural and magnetic properties of crystalline zinc-substituted cobalt ferrite nanoparticles, $Zn_xCo_{1-x}Fe_2O_4$ with $x = 0, 0.25, 0.5, 0.75,$ and 1 , prepared by hydrothermal method. The structural and magnetic properties of these nanoparticles were investigated by XRD, TEM, FTIR, and VSM. All the ferrite nanoparticles were prepared with sizes smaller than 20 nm, thus lying within the range of single-domain regime. The results of Rietveld refinement revealed that all prepared nanoparticles were cubic and single phase, and the increase in Zn concentration resulted in an increase in the lattice constant, x-ray density, and the average bond length on tetrahedral sites. The TEM measurements showed that the nanoparticles were monodisperse and spherical in shape. All FTIR spectra of the prepared ferrites showed two dominant absorption bands, thus confirming the formation of single-phase spinel structure with two sub-lattices: tetrahedral (A-site) and octahedral (B-site). The room temperature M versus H magnetization measurements revealed that the ferrite nanoparticles were ferromagnetic for $x = 0$ and superparamagnetic for $x \geq 0.25$. At 10 K, all ferrite nanoparticles showed ferrimagnetic behavior that is weakened by Zn substitution. The saturation magnetization and the first anisotropy constant were observed to decrease with increasing Zn concentration. The zero field cooled and field cooled magnetization data revealed that both superparamagnetic and spin-glass like states may coexist together depending on amount of Zn concentration and temperature.

Keywords Spinel ferrites · Rietveld refinement · Magnetization · Superparamagnetism · Spin-glass · LA model

1 Introduction

Magnetic ferrites are a group of materials that contain iron oxide as a major constituent. They have been investigated intensively during the past few decades as they can be utilized in several applications such as permanent magnets, chemical sensors, high density recording systems, microwave devices, and biomedical applications [1–5].

Spinel ferrites, a class of magnetic ferrites, crystallize into a cubic spinel type structure with a space group $Fd\bar{3}m$ and have the general molecular formula AB_2O_4 , where A^{2+} and B^{3+} are the divalent and trivalent cations, respectively [6]. The unit cell of spinel structure is composed of eight formula units $[AB_2O_4]_8$, allowing 56 ions to be incorporated in the large unit cell [7]. The structural and magnetic properties of spinel ferrites depend on several factors such as synthesis method, chemical composition, and cations distribution between the tetrahedral (A sites) and octahedral (B sites). The last factor plays a major role in determining the magnetic properties of these ferrites, resulting in a wide range of possible distributions of cations between the A and B sites [8].

Among various types of spinel ferrites, cobalt ferrite $CoFe_2O_4$ is of a particular importance as it exhibits some exceptional physical and chemical properties, such as high coercivity, large magnetic anisotropy, moderate saturation magnetization, high resistivity, and good mechanical and

✉ Gassem M. Alzoubi
Gassem@hu.edu.jo

¹ Department of Physics, The Hashemite University, Zarqa 13115, Jordan

² Department of Physics, Kuwait University, 13060 Safat, Kuwait

³ Department of Physics, Jordan University of Science and Technology, Irbid 22110, Jordan

⁴ Department of Physics, Al al-Bayt University, Mafraq 13040, Jordan

chemical stabilities [9, 10]. Ideal cobalt ferrite has an inverse spinel structure, where all Co cations occupy the octahedral site and the Fe cations are equally distributed in both tetrahedral and octahedral sites that can be represented by the formula $(\text{Fe}^{3+})_A[\text{Co}^{2+}\text{Fe}^{3+}]_B\text{O}_4$. The magnetic properties of cobalt ferrites can be tuned by controlled substitution. Replacing the magnetic Co ions, for example, by the non-magnetic Zn ions in a controlled manner can drastically change the magnetic properties of the cobalt ferrite nanoparticles.

There are several synthesis methods used to fabricate magnetic ferrite nanoparticles, such as the sol-gel method [11], the co-precipitation method [12], the ceramic technique [13], the hydrolysis method [14], the hydrothermal method [15], and the mechanical alloying method [16].

One of the most interesting magnetic properties of ferrite nanoparticles is the size dependence of their ferrimagnetism. As particle size decreases to typically 40 nm, the particle can not be broken into domains, and hence remains with a single domain [17]. Based on the variation of coercivity as a function of particle size at RT and 10 K, it was also reported that a single-domain size limit of cobalt ferrite nanoparticles prepared by coprecipitation method was found around 40 nm [18]. Since it is very difficult to produce particles with narrow size distribution, determining the critical single-domain size of ferrite nanoparticles is not an easy task and is rarely discussed in the literature. Further reduction of the size of the particle to below 20 nm leads to the transformation from ferrimagnetic state to superparamagnetic state at specific temperature called the blocking temperature (T_B). In this superparamagnetic regime and even at very low temperatures, the thermal fluctuations energy can easily overcome the magnetic anisotropy energy barrier of the nanoparticle, and hence randomize its magnetic moment, resulting in losing ferrimagnetism of the nanoparticle. The coexistence of both superparamagnetic and single-domain nanoparticles would affect the coercivity values and further complicates the estimation of the critical single-domain size, making it an approximate one.

Most of previous works done on cobalt ferrites and their doped families were in the multi-domain regime in which a typical size of synthesized nanoparticles was bigger than 40 nm, and hence negligible size dependence of their magnetic properties [19]. This is because fabrication of ultra small and monodisperse nanoparticles is considered a challenge in this field. On the other hand, most studies conducted on ferrite systems lying in the single-domain regime investigated and described the possible existence of either superparamagnetism or spin-glass behavior and addressed these two phenomena as a separate topics. The intention behind the present work is to investigate the possible coexistence of both superparamagnetism and spin-glass behavior in zinc-substituted cobalt ferrite nanoparticles prepared by

hydrothermal method. The main goal is to produce ultra small and monodisperse nanoparticles that lie within the single-domain regime and to make a detailed systematic study on their structural and magnetic properties. Having a reproducible recipe of making these stable ferrite nanoparticles in the single-domain regime and understanding their magnetic properties is an important issue toward utilizing them in several applications, mainly in data storage, magnetic recording, and biomedical applications [20–22].

2 Materials and methods

Cobalt (II) nitrate hexahydrate $\text{Co}(\text{NO}_3)_2 \cdot 6\text{H}_2\text{O}$ (Reagent grade, 98%), zinc nitrate hexahydrate $\text{Zn}(\text{NO}_3)_2 \cdot 6\text{H}_2\text{O}$ (Laboratory reagent, 98%), Iron (III) nitrate nonhydrate $\text{Fe}(\text{NO}_3)_3 \cdot 9\text{H}_2\text{O}$ (Analytical reagent, $\geq 98\%$), Sodium hydroxide NaOH (Reagent grade, $\geq 98\%$), HPLC plus DI water, Ethanol absolute anhydrous (ACS reagent) were used as starting materials without further processing. All chemicals were bought from Sigma-Aldrich. We used different amounts of the starting materials according to the required stoichiometric proportions of the $\text{Zn}_x\text{Co}_{1-x}\text{Fe}_2\text{O}_4$ with $x = 0, 0.25, 0.5, 0.75, \text{ and } 1$. In this work, we followed the recipe of Amanda et al. for hydrothermal synthesis with smart modification [23]. In this work, 10 mmol of Fe(III) nitrate, 5 mmol of a mixture of cobalt nitrate and zinc nitrate, were dissolved in 140 mL of DI water and magnetically stirred at 500 rpm for 10 min. Then a precipitating agent solution of 60 mmol of NaOH dissolved in 20 mL DI water was added drop wise into the above cationic solution under vigorous magnetic stirring (~ 1500 rpm). The molarity of nitrates was kept below 0.12 mol/L in order to get nearly monodisperse nanocrystals.

The final solution was allowed to stir at ~ 1500 rpm for 15 minutes. The solution was then transferred to a 200 mL Teflon-lined stainless steel autoclave, subsequently sealed, placed in a vacuum oven, and heated to 190°C for 12 h, after which the autoclave was taken outside the vacuum oven and left to cool down naturally to room temperature. The resulting product was washed twice with ethanol and three times with DI water, where after each washing step the nanoparticles were collected by a strong magnet. Then, the nanoparticles were dispersed in 15 mL of DI water, isolated by centrifugation at 4800 rpm, dried in a vacuum oven at 105°C for 24 h, and finally crushed using mortar and pestle, thereby yielding ~ 1.1 g of each sample. Finally, the nanoparticles were annealed at 700°C for 6 h. Annealing at 700°C is sufficient enough to enhance the crystallinity and magnetic properties of the ferrites being prepared. Higher annealing temperatures, however, have been avoided as they may induce particle growth beyond the limit of single-domain size and therefore lowers the coercivity.

The prepared nanoparticles were characterized by various techniques. The X-ray diffraction (XRD) measurements were performed using Rigaku Ultima IV with $\text{CuK}\alpha$ radiation ($\lambda = 1.5406 \text{ \AA}$) diffractometer, in the range of $2\theta = 16^\circ - 70^\circ$, with a scanning rate of 2° per minute. The structural analysis including Rietveld refinement of XRD patterns was performed using the FullProf program. The morphology and microstructure of the ferrite nanoparticles were characterized using JEOL 1200 transmission electron microscope (TEM). The Fourier-transform infrared spectroscopy (FTIR) was utilized to obtain the infrared spectra of samples using a Bruker Vertex 70 FTIR spectrometer in the range of $370\text{--}900 \text{ cm}^{-1}$. Magnetic measurements were collected using Quantum Design Physical Property Measurement System (PPMS), that is equipped with Vibrating Sample Magnetometer (VSM), in the temperature range $10\text{--}300 \text{ K}$ and in a vertical magnetic field up to 25 kOe .

3 Results and discussion

3.1 X-ray diffraction and structural analysis

XRD patterns for the $\text{Zn}_x\text{Co}_{1-x}\text{Fe}_2\text{O}_4$ ferrites with $x = 0, 0.25, 0.5, 0.75,$ and 1 are shown in Fig. 1. All peaks were indexed according to the space group $\text{Fd}\bar{3}\text{m}$ with planes: (111), (220), (311), (222), (400), (422), (511), and (440), thus confirming the single phase nature of cubic spinel structure, without any impurity phases. All diffraction peaks are well matched with the standard powder diffraction data of spinel ferrites of CoFe_2O_4 (PDF # 22-1086) and ZnFe_2O_4 (PDF # 73-1963) that are shown as a vertical black bars at the bottom of the figure. The broad XRD lines indicate that these particles are in the nanosize range.

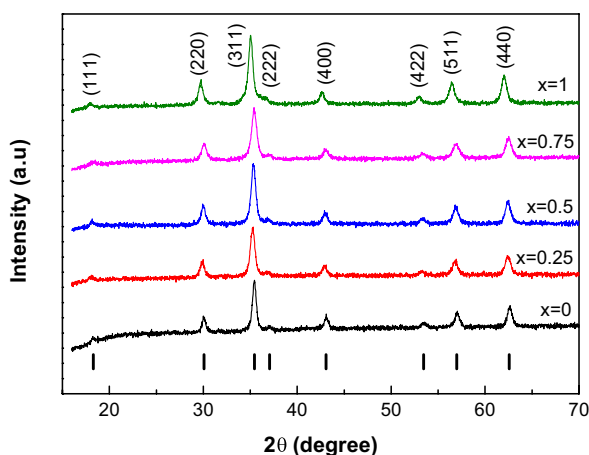


Fig. 1 (Color online) XRD patterns of the $\text{Zn}_x\text{Co}_{1-x}\text{Fe}_2\text{O}_4$ ferrites with $x = 0, 0.25, 0.5, 0.75,$ and 1 . Bragg reflections are represented by a vertical black bars at the bottom

All XRD patterns were analyzed using the FullProf software by employing Rietveld refinement technique [24]. The refinement process was performed as follows. Specimen displacement, background, and scale factor were refined first. Next, unit cell dimensions, atomic coordinates, and profile parameters were refined. After each refinement trial, the Rietveld fitting quality was checked using the reliability R -factors (expected R_{exp} , profile R_p and weighted profile R_{wp}) that must reach their minimum values and the goodness of fit ($\text{GoF} = (R_{\text{wp}}/R_{\text{exp}})^2$) that must approach one from above. Before starting Rietveld refinement, cations and anions positions, and site occupancy (for both tetrahedral site (8a) and octahedral site (16d)) were determined carefully. In general, there are two choices for the origin of the unit cell in spinel ferrites [25]. The first choice is to have the origin placed at the tetrahedral A-site cation (with point symmetry of $= 43 \text{ m}$). The second choice is to have the origin placed at an octahedral vacancy (with point symmetry of $= 3 \text{ m}$). In this work, we followed the second choice. Assuming that an inverse spinel structure for cobalt ferrites and a normal spinel structure for zinc ferrites, [25–27], all cations were distributed between the tetrahedral and octahedral sites so as to preserve the stoichiometric composition of the $\text{Zn}_x\text{Co}_{1-x}\text{Fe}_2\text{O}_4$ ferrites. Table 1 summarizes the Wyckoff positions, atomic coordinates (x, y, z), and site occupancy (sof) used in the Rietveld refinement of the $\text{Zn}_x\text{Co}_{1-x}\text{Fe}_2\text{O}_4$ ferrites.

Figure 2 shows a typical Rietveld refinement for the $\text{Zn}_x\text{Co}_{1-x}\text{Fe}_2\text{O}_4$ ferrites with $x = 0.5$. As shown in the figure, there is an excellent agreement between the observed data and the calculated one. The outcomes of the refinement for this sample as well as for the other samples are summarized in Table 2. The main four refined quantities were the oxygen positional parameter u , the experimental lattice parameter a_{exp} , the d_{hkl} -spacing, and the full width at half maximum (FWHM). These quantities were used to calculate the x-ray density d_x , the theoretical lattice parameter a_{thy} , the crystallite size D , and the bond lengths at the tetrahedral R_A and octahedral R_B sites. The ideal value of u is 0.25 \AA , assuming that the oxygen anions form a perfect cubic closed packing (CCP) lattice and the origin of the unit cell is placed at an octahedral vacancy [25]. However, in real spinel ferrites, oxygen anions are slightly shifted away from their ideal CCP positions resulting in remarkable implications on bond lengths and angles. As shown in Table 2, the value of u changes from 0.2564 \AA for $x = 0$, representing pure cobalt ferrite (CoFe_2O_4), to 0.2731 \AA for $x = 1$, representing pure zinc ferrite (ZnFe_2O_4). These measured values of u are consistent with reported values of 0.2556 \AA and 0.2582 \AA for CoFe_2O_4 [27] and ZnFe_2O_4 [28], respectively.

The estimated experimental lattice constant (a_{exp}), as shown in Fig. 3a, is observed to increase from 8.371 \AA to 8.426 \AA with the increase in Zn concentration in all samples.

Table 1 Wyckoff positions (Tetrahedral site (8a), Octahedral site(16d), Oxygen site(32e)), atomic coordinates (x, y, z), and site occupancy (sof) used in Rietveld refinement of the $Zn_xCo_{1-x}Fe_2O_4$ ferrites

x	Atom	(8a)			(16d)			(32e)			sof
		xyz	xyz	xyz	xyz	xyz	xyz	xyz			
0	Co	-	-	-	1/2	1/2	1/2	-	-	-	0.5
	Fe	-	-	-	1/2	1/2	1/2	-	-	-	0.5
	Fe	1/8	1/8	1/8	-	-	-	-	-	-	1
	O	-	-	-	-	-	-	1/4	1/4	1/4	1
0.25	Co	-	-	-	1/2	1/2	1/2	-	-	-	0.375
	Fe	-	-	-	1/2	1/2	1/2	-	-	-	0.625
	Fe	1/8	1/8	1/8	-	-	-	-	-	-	0.75
	O	-	-	-	-	-	-	1/4	1/4	1/4	1
0.5	Zn	1/8	1/8	1/8	-	-	-	-	-	-	0.25
	Co	-	-	-	1/2	1/2	1/2	-	-	-	0.25
	Fe	-	-	-	1/2	1/2	1/2	-	-	-	0.75
	Fe	1/8	1/8	1/8	-	-	-	-	-	-	0.5
0.75	O	-	-	-	-	-	-	1/4	1/4	1/4	1
	Zn	1/8	1/8	1/8	-	-	-	-	-	-	0.5
	Co	-	-	-	1/2	1/2	1/2	-	-	-	0.125
	Fe	-	-	-	1/2	1/2	1/2	-	-	-	0.875
1	Fe	1/8	1/8	1/8	-	-	-	-	-	-	0.25
	O	-	-	-	-	-	-	1/4	1/4	1/4	1
	Zn	1/8	1/8	1/8	-	-	-	-	-	-	0.75
	Fe	-	-	-	1/2	1/2	1/2	-	-	-	1
1	O	-	-	-	-	-	-	1/4	1/4	1/4	1
	Zn	1/8	1/8	1/8	-	-	-	-	-	-	1

Table 2 Results of Rietveld refinement of all XRD patterns of the $Zn_xCo_{1-x}Fe_2O_4$ ferrites with $x = 0, 0.25, 0.5, 0.75,$ and 1 . Average crystallite size D , x-ray density d_x , R-factors (R_{exp} , R_p , R_{wp}) and goodness of fit (GoF), cell parameter a , oxygen position parameter u , tetrahedral bond length R_A , and octahedral bond length R_B

x	0	0.25	0.5	0.75	1
D (nm)	17.4	14.4	14.4	12.3	15.0
d_x (g/cm³)	5.31	5.34	5.34	5.36	5.35
<i>Residual factors (%)</i>					
R_{exp}	1.261	1.307	1.312	1.482	1.537
R_p	1.036	1.075	1.096	1.223	1.368
R_{wp}	1.303	1.364	1.378	1.548	1.720
GoF (χ^2)	1.07	1.09	1.10	1.09	1.25
<i>Cell parameters (Å)</i>					
a_{thy}	8.3829	8.4084	8.4055	8.4004	8.457
a_{exp}	8.3706	8.3765	8.3942	8.4019	8.4263
u	0.2564	0.2667	0.2691	0.2698	0.2731
R_A	1.9051	2.0559	2.0951	2.1072	2.1615
R_B	2.0405	1.9642	1.9514	1.9484	1.9316

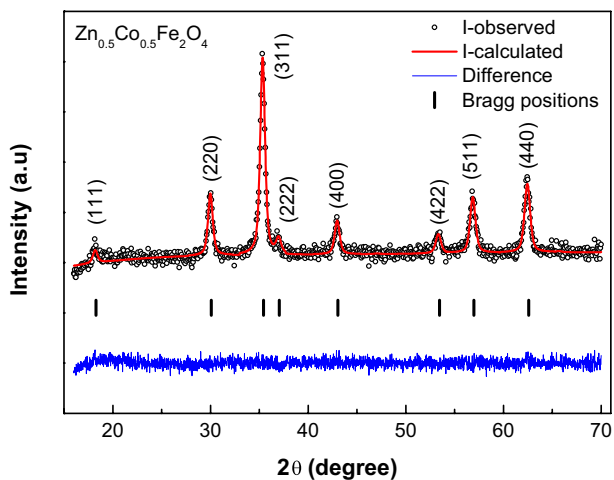


Fig. 2 (Color online) Rietveld refined XRD pattern of the $Zn_xCo_{1-x}Fe_2O_4$ ferrites with $x = 0.5$. The figure includes experimental data (black circles), calculated data (red line), the difference between experimental and calculated data (blue line), and Bragg reflections (vertical bars)

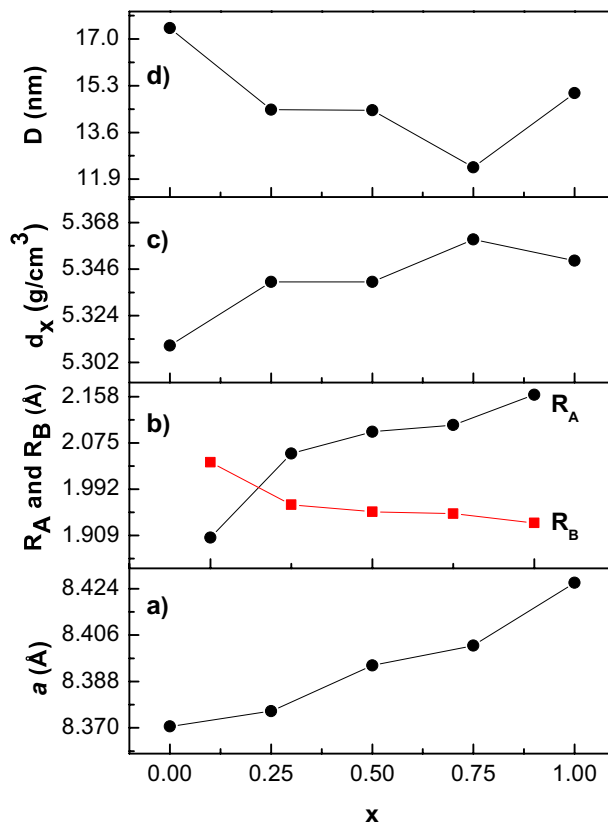


Fig. 3 (Color online) The behavior of some Rietveld refined quantities as a function of Zn concentration: **a** lattice constant, **b** the average bond lengths of R_A and R_B , **c** the x-ray density, and **d** the crystallite size

The replacement of Co^{2+} ions of radius (0.76 Å) with Zn^{2+} ions of bigger radius (0.81 Å) leads to increase in the lattice constant, consistent with Vegard's law [29]. These measured values of a_{exp} for the two end samples agree with reported results of 8.373 Å [30] for CoFe_2O_4 and 8.430 Å [31] for ZnFe_2O_4 , respectively. The lattice constant can also be calculated from $a_{\text{thy}} = d_{hkl} \sqrt{h^2 + k^2 + l^2}$. The lattice constant was calculated using the d_{440} plane as high angle diffraction peaks give better estimate than those low angle ones.

The average bond lengths at the tetrahedral (R_A) and octahedral (R_B) sites can be calculated using the relations [8]

$$R_A = a_{\text{exp}} \sqrt{3} (u - 0.125) \quad (1)$$

$$R_B = a_{\text{exp}} \sqrt{2} (3u^2 - 2u + 0.375) \quad (2)$$

The refined values of R_A and R_B with Zn concentration are shown in Fig. 3b. The R_A is observed to increase with Zn concentration. This is due to the substitution of Fe^{3+} ions with radius (0.66 Å) at the tetrahedral A-site by the larger radius (0.81 Å) Zn^{2+} ions. On the other hand, the R_B is observed to decrease with Zn concentration. This is due to the substitution of Co^{2+} ions with radius (0.76 Å) at the octahedral B-site by the smaller radius (0.66 Å) Fe^{3+} ions that migrate from the A site to the B site. This behavior of R_A and R_B should be linked to the behavior of the parameter u . As u changes, the anion sublattice expands or contracts until the volumes of the A- and B-sites match the radii of the constituent cations [25].

The x-ray density d_x was calculated using the relation

$$d_x = ZM/Na^3 \quad (3)$$

where Z is the number of molecules per unit cell ($Z = 8$), M is molecular weight, N is Avogadro's number, and a^3 is volume of the unit cell. The refined values of d_x for all samples are shown in Table 2 and plotted in Fig. 3c as a function of Zn concentration. As can be seen from the figure, the density is observed to increase with Zn concentration for nanoparticles with $x = 0, 0.25, 0.5,$ and 0.75 . This is attributed to the heavier weight of a zinc atom as compared to that of cobalt atom. However, for the $x = 1$ (ZnFe_2O_4) nanoparticles, the density decreases to 5.35 g/cm^3 . This can be understood by realizing that the density is directly proportional to the mass of the Zn atom and inversely proportional to the volume of the unit cell. Therefore, the significant increase in the size of the unit cell, due to the increase in the lattice constant, can not be compensated by the increase in the mass of Zn atom.

The crystallite size D was evaluated by the Scherrer equation

$$D = \frac{K\lambda}{\beta \cos \theta} \quad (4)$$

where $K = 0.89$, λ is the wavelength of the x-ray radiation ($\lambda = 1.5406 \text{ Å}$), θ is the diffraction angle of the most intense peak (311) and β is its full width at half maximum (FWHM) in radian. The calculated values of D for all ferrite nanoparticles are shown in Table 2 and plotted in Fig. 3d as a function of Zn concentration. It is clear that all prepared ferrite nanoparticles have sizes lying within the single-domain regime, i.e., below 40 nm. The size of the nanoparticles is observed to slightly decrease with Zn concentration. This may be explained by looking at the electronic configuration of $\text{Co}^{2+} (3d^7)$ that has more tendency to interact with ligands and oxygen anions, as compared to $\text{Zn}^{2+} (3d^{10})$, which has a complete electronic configuration [32].

3.2 TEM analysis

Figure 4 shows TEM images and particle size distributions for the $\text{Zn}_x\text{Co}_{1-x}\text{Fe}_2\text{O}_4$ spinel ferrites with $x = 0, 0.25, 0.5, 0.75,$ and 1 taken at high magnification of 250,000. As can be seen from the figure, the nanoparticles are roughly spherical in shape, indicating that the followed recipe was successful in producing monodisperse spherical nanoparticles. As shown in the figure, the estimated average particle size of all ferrite nanoparticles obtained from TEM measurements is nearly twice the average crystallite size obtained from XRD measurements (see Table 2). Similar behavior was observed for the same system synthesized by coprecipitation method, where the average particle size was found almost three times larger than the average crystallite size [31]. Such difference is expected as with XRD one measures the average crystallite size, whereas with TEM one measures the average particle size which can be made of several crystallites, this is why particle size has to be always bigger than crystallite size.

3.3 FTIR analysis

Figure 5 shows the recorded FTIR spectra for $\text{Zn}_x\text{Co}_{1-x}\text{Fe}_2\text{O}_4$ ferrites in the wave number range of 370–900 cm^{-1} . For ferrites with spinel type structure, it is expected to have four modes of vibrations occurring in the ν_1 (650–550 cm^{-1}), ν_2 (525–490 cm^{-1}), ν_3 (380–335 cm^{-1}) and ν_4 (300–200 cm^{-1}) regions [33]. As can be seen from the figure, two main metal-oxygen bands are seen at frequencies ~ 556 and 410 cm^{-1} . The higher frequency band is caused by the stretching vibrations of metal-oxygen bond in the tetrahedral (A sites). The lower frequency one is caused by the metal-oxygen vibrations in the octahedral (B sites). These absorption bands confirm the formation of single-phase spinel structure with two sub-lattices: tetrahedral and octahedral [19, 34]. As seen in the figure, all ferrite samples show shoulder peaks in the tetrahedral region occurring $\sim 615 \text{ cm}^{-1}$, indicating that the tetrahedral site is always occupied by more than one cation. It can therefore be deduced that the

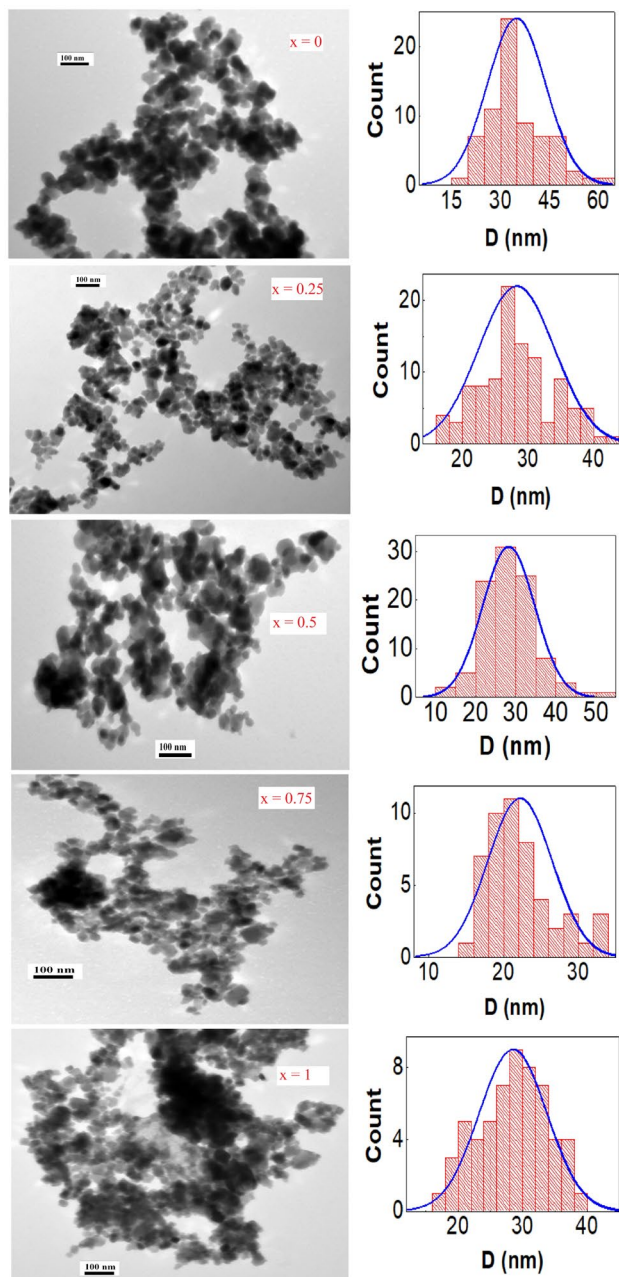


Fig. 4 (Color online) TEM images and particle size distributions for the $Zn_xCo_{1-x}Fe_2O_4$ spinel ferrites with $x = 0, 0.25, 0.5, 0.75,$ and 1 taken at high magnification of $250,000\times$

synthesized ferrite nanoparticles are most likely mixed spinel-type structures. The high frequency peak is observed to shift to low frequency regions; $556, 556, 553, 549, 532\text{ cm}^{-1}$ as a function of Zn concentration. This is consistent with the increase in the value of the bond length at the tetrahedral site, R_A , observed in XRD analysis (see Table 1). In addition, the absorption bandwidth of the high-frequency peak is observed to decrease slightly with increasing concentration of Zn, indicating that the absorption of infrared radiation

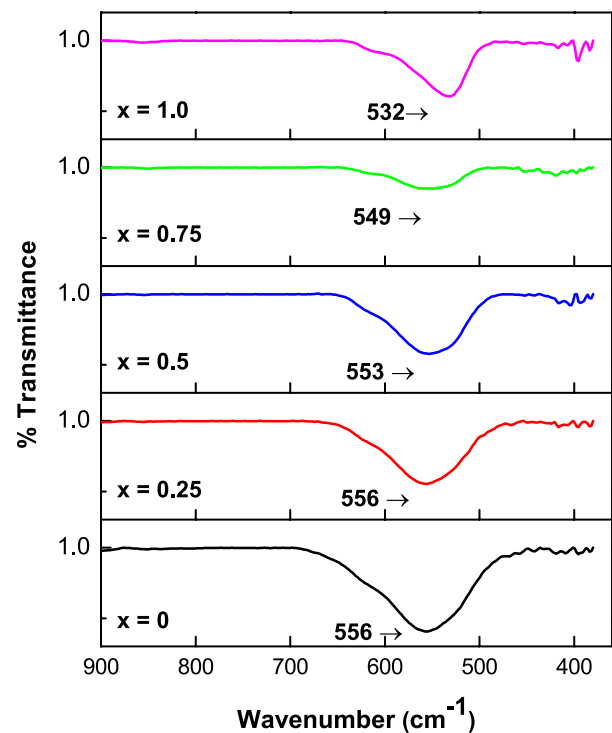


Fig. 5 (Color online) FTIR absorption bands for the $Zn_xCo_{1-x}Fe_2O_4$ spinel ferrites with $x = 0, 0.25, 0.5, 0.75,$ and 1 measured in the wave number range of $370\text{--}4000\text{cm}^{-1}$

becomes more selective when cobalt is substituted by zinc. The ν_3 and ν_4 absorption bands could not be observed as they are located in the far-infrared region, which is beyond the measuring range of the FTIR machine used in recording the FTIR spectra.

3.4 Magnetic properties

Two types of magnetic measurements were taken systematically on $Zn_xCo_{1-x}Fe_2O_4$ ferrite nanoparticles. The first is recording the magnetization versus magnetic field at two temperatures 300 K and 10 K . The second is recording the magnetization versus temperature in the presence of small applied magnetic field (100 Oe) in order to generate the zero field cooled (ZFC) and the field cooled (FC) magnetization curves.

Figure 6 shows magnetization curves of the $Zn_xCo_{1-x}Fe_2O_4$ ferrites with $x = 0, 0.25, 0.5, 0.75,$ and 1 , measured at 300 K and 10 K , in which the magnetic field was swept from -25 kOe to 25 kOe . As shown in the figure, the hysteresis behavior of the parent ferrite ($CoFe_2O_4$) is affected by the successive addition of Zn ions, resulting in reduction of both saturation magnetization and coercivity. Such a decrease in coercivity is expected as the magnetic Co ions are continuously replaced by the non-magnetic Zn ions.

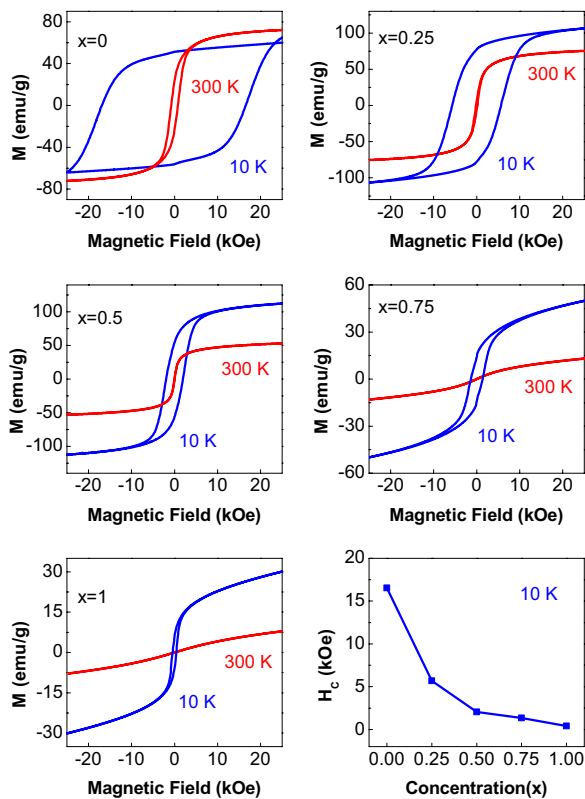


Fig. 6 (Color online) Magnetization curves of the $\text{Zn}_x\text{Co}_{1-x}\text{Fe}_2\text{O}_4$ ferrites with $x = 0, 0.25, 0.5, 0.75,$ and 1 , measured at 300 K and 10 K . The figure in the bottom right corner represents the variation of the coercive field (at 10 K) with Zn concentration

Actually, it is quite evident that at room temperature, the substitution process produced a change from ferrimagnetism to superparamagnetism as x evolved from 0 to 1 . Furthermore and based on the shape of the hysteresis loops, one can see the existence of either ferrimagnetic or superparamagnetic phases depending on the amount of Zn concentration. At room temperature, the $x = 0$ parent cobalt ferrite nanoparticles exhibit ferromagnetic behavior with well-defined saturation magnetization ($M_s \sim 70\text{ emu/g}$), coercivity ($H_c \sim 800\text{ Oe}$), and remanence ($M_r \sim 24\text{ emu/g}$). For all other room temperature ferrite nanoparticles with $x \geq 0.25$, the corresponding $M-H$ curves show superparamagnetic behavior that is demonstrated by the sigmoidal shape of their corresponding $M-H$ curves with nearly zero hysteresis. However, at 10 K , all ferrite nanoparticles showed ferrimagnetic behavior that is weakened by Zn substitution. This is evident from the reduction in the coercivity from $\sim 16.5\text{ kOe}$ for $x = 0$ to $\sim 0.4\text{ kOe}$ for $x = 1$ as shown in the bottom right corner of Fig. 6.

It is clear from Fig. 6 that the magnetization is not saturated using the maximum applied field of 25 kOe . Therefore, we utilized the law of approach (LA) to saturation to

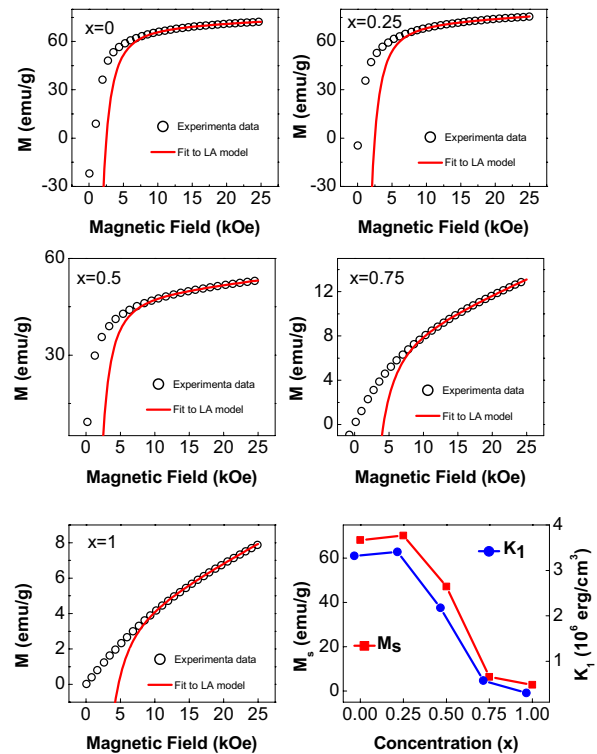


Fig. 7 (Color online) Room temperature magnetization curves of the $\text{Zn}_x\text{Co}_{1-x}\text{Fe}_2\text{O}_4$ ferrites with $x = 0, 0.25, 0.5, 0.75,$ and 1 , fitted to LA model. The figure in the bottom right corner represents the variation of saturation magnetization (M_s) and first anisotropy constant (K_1) with Zn concentration

determine the saturation magnetization (M_s) and the first anisotropy constant (K_1). The LA approach describes the magnetic field dependence of magnetization near saturation and it is usually valid at fields much higher than the coercive field ($H \gg H_c$) [35]. The magnetization near the saturation is given by [35]

$$M = M_s \left(1 - \frac{b}{H^2}\right) + \kappa H \quad (5)$$

where $b = \frac{8}{105} \frac{K_1^2}{\mu_0^2 M_s^2}$, M is the magnetization, M_s is the saturation magnetization, H is the applied magnetic field, μ_0 is the magnetic permeability of free space, and K_1 is the first anisotropy constant (also called the cubic anisotropy constant). The last term, κH , is known as the forced magnetization which represents the linear increase in the spontaneous magnetization at high fields. We observed that this term was necessary to fit the obtained data. Figure 7 shows room temperature magnetization curves of the $\text{Zn}_x\text{Co}_{1-x}\text{Fe}_2\text{O}_4$ ferrites with $x = 0, 0.25, 0.5, 0.75,$ and 1 , fitted to the LA model. As shown in the figure, the LA model describes well the magnetization at high fields, therefore our fit was restricted to magnetization data taken from 10 to 25 kOe . The obtained

values of M_s and K_1 from the fit as well as the values of H_c and M_r are summarized in Table 3. The variation of M_s and K_1 with Zn concentration is shown in the bottom right corner of Fig. 7. Both M_s and K_1 slightly increase from $x = 0$ to $x = 0.25$, and then decrease for all particles with $x > 0.25$ (as discussed latter). The measured values of M_s and H_c at 300 K for $x = 0$ are close to the room temperature (RT) reported values of 74.5 emu/g and 0.85 kOe, respectively [23]. The measured values of K_1 for $x = 0$ and $x = 1$ are close to the RT reported values of 3.8×10^6 and 0.2×10^6 erg/cm³ for CoFe₂O₄ [36] and ZnFe₂O₄ [37], respectively. It is evident from Table 3 that when x changes from 0.5 to 0.75, the M_s value has fallen sharply from ~ 47 emu/g to ~ 6 emu/g. Similar behavior was observed in the Zn_xCo_{1-x}Fe₂O₄ ferrites synthesized by sol-gel method and annealed between 500 °C and 900 °C, where the M_s value dropped from ~ 50 emu/g to ~ 10 emu/g when x changed from 0.5 to 0.75 [34]. The LA model was applied only to room temperature magnetization data. Applying this model to low temperature data, mainly at 10 K, does not give reasonable results due to higher value of coercive field compared with that at room temperature, thereby making the validity condition ($H \gg H_c$) is not fulfilled [35].

The distribution of cations between the tetrahedral (A-site) and octahedral (B-site) plays an important role in determining magnetic properties of spinel ferrites. The distribution of cations can be expressed as $(Zn_x^{2+} Fe_{(1-x)}^{3+})_A [Co_{(1-x)}^{2+} Fe_{(1+x)}^{3+}]_B O_4^{2-}$. Based on Neel's two sublattice model of ferrimagnetism [31], the magnetic moments of ions at the A and B sites are aligned antiparallel to each other and the expected net magnetic moment per formula unit reads $n_B(x) = M_B(x) - M_A(x)$, where $M_B(x)$ and $M_A(x)$ are the B and A sublattice magnetic moments in μ_B . Using the ionic magnetic moments of Fe³⁺, Co²⁺, and Zn²⁺ as $5\mu_B$, $3\mu_B$, and $0\mu_B$, respectively, the obtained values of the expected magnetic moments read $3\mu_B$, $4.75\mu_B$, $5.8\mu_B$, $8.25\mu_B$, and $10\mu_B$, for the corresponding Zn concentrations of 0, 0.25, 0.5, 0.75, and 1, respectively. It is clear from these values that the magnetic moment (and hence

magnetization) increases as a function of Zn concentration, in agreement with the observed magnetization increase from $x = 0$ to $x = 0.25$. The Zn²⁺ ions prefer to occupy the A sites, so as x increases from 0 to 0.25, more Fe³⁺ ions are migrated to the B sites, resulting in a decrease in the magnetic moment of the A sites and an increase in the magnetic moment of the B sites [34]. Hence, the overall magnetization increases. On the other hand, the measured magnetization of the $x > 0.25$ ferrites is observed to gradually decrease with further increase in Zn concentration, indicating that the Neel's model is unable to describe the decrease in magnetization of the $x > 0.25$ ferrite samples. Similar behavior has also been observed in previously studied Zn_xCo_{1-x}Fe₂O₄ ferrites [31, 34, 38]. The decrease in magnetization for $x > 0.25$ is attributed to the possible existence of non-collinear spin arrangement in the system, which can be explained on the basis of the three-sublattice model suggested by Yafet and Kittel [38]. With further increase of Zn²⁺ ions, more Fe³⁺ ions are migrated to the B sites, resulting in an increase in the B–B super-exchange interactions. The enhanced B–B interactions result in the formation of random spin canting on the B sites, which in turn decreases the net magnetic moment (and hence net magnetization).

The ZFC-FC Magnetization curves were obtained by the well-known procedure described in reference [39]. Figure 8 shows the ZFC-FC Magnetization curves of the Zn_xCo_{1-x}Fe₂O₄ ferrites with $x = 0, 0.25, 0.5, 0.75$, and 1 measured under an applied small magnetic field of 100 Oe. It is clear from the figure that the parent cobalt ferrite is in a single ferromagnetic phase over the whole temperatures range. This is consistent with the corresponding M – H curves taken at 300 K and 10 K (see Fig. 6). The ZFC-FC Magnetization curves of the parent ferrite can be understood as follows. When the nanoparticle is cooled in zero field, its magnetization aligns with the direction of the easy axis and can not be changed further due to the existence of the magnetic anisotropy energy barrier that is being enhanced with reducing temperature. Since the orientations of the easy axes of the nanoparticles are random, the net magnetization approaches zero at very low temperatures. Now, when the nanoparticles are warmed up to 300 K in the presence of the field, they will gain a thermal energy sufficient to switch their magnetizations from the easy axes to the direction of the applied field, leading to an increase in the overall magnetization of the sample, as shown in the $x = 0$ ZFC portion of Fig. 8. For the FC measurements and as temperature is reduced, the magnetic moment of each nanoparticle will tend to align with the easy axis that is closest to the applied field direction, and will remain locked in that direction. As can be seen, the shape of the FC curve is rather flat, which is a signature of spin-glass like behavior resulting from non-negligible dipole-dipole interactions between the ferromagnetic nanoparticles [40–42].

Table 3 Coercivity (H_c), remanent magnetization (M_r), saturation magnetization (M_s), and first anisotropy constant (K_1) of the Zn_xCo_{1-x}Fe₂O₄ ferrites with $x = 0, 0.25, 0.5, 0.75$, and 1 measured at room temperature

x	H_c (kOe)	M_r (emu/g)	M_s (emu/g)	K_1 (erg/cm ³)
0	0.77	24.1	68.1	3.3×10^6
0.25	0.19	5.8	70.1	3.4×10^6
0.5	0.02	1.1	47.2	2.2×10^6
0.75	0.01	0.02	6.4	0.6×10^6
1	0	0	2.8	0.3×10^6

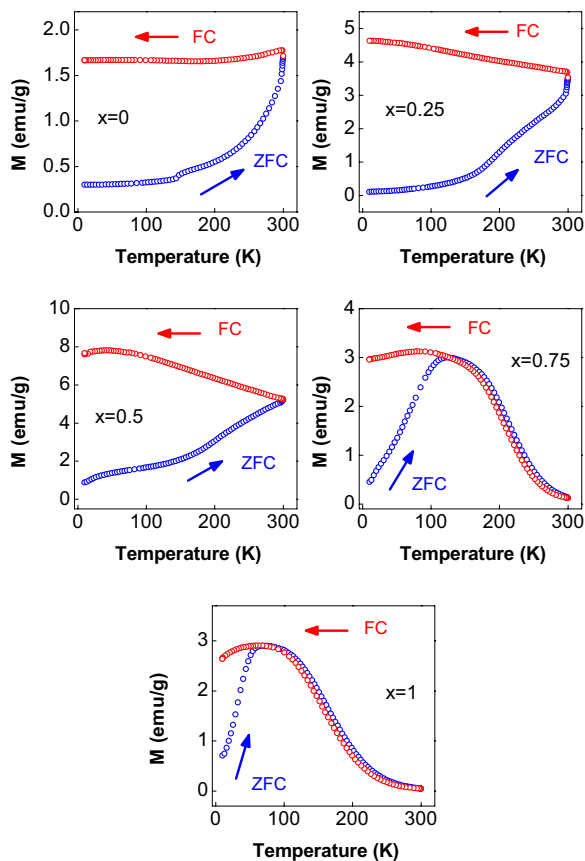


Fig. 8 (Color online) ZFC-FC Magnetization curves of the $\text{Zn}_x\text{Co}_{1-x}\text{Fe}_2\text{O}_4$ ferrites with $x = 0, 0.25, 0.5, 0.75,$ and 1 , measured with an applied magnetic field of 100 Oe

The ZFC branches of the $x = 0.25$ and $x = 0.5$ ferrite nanoparticles are almost similar to the corresponding ZFC branch of the $x = 0$ one. However, the FC branch of the $x = 0.25$ ferrite nanoparticles shows a continuous increase with reducing temperature with no tendency to reach saturation, indicating that the ferrite nanoparticles are non-interacting and superparamagnetic in this temperature range [42]. The FC branch of the $x = 0.5$ ferrite nanoparticles also shows a continuous increase with reducing temperature down to around 80 K, indicating that the ferrite nanoparticles are non-interacting and superparamagnetic from 300 K down to 80 K. Below 80 K, the FC curve starts to saturate indicating the formation of spin-glass layer on the surface of the nanoparticles.

As shown in Fig. 8, the ZFC curve of $x = 0.75$ ferrite nanoparticles shows a peak around 150 K. This peak results from both superparamagnetic behavior (with blocking temperature T_B) and spin-glass like behavior (with freezing temperature T_g). Here, it is impossible to distinguish T_B from T_g as they are overlapped. However, the superparamagnetic behavior is evident by the Curies

law-like behavior above T_B . By further increasing the temperature above T_B , the thermal energy exceeds the magnetic anisotropy energy, and hence the nanoparticles will gain sufficient thermal energy that is able to randomize their moments, resulting in reducing the overall magnetization of these ferrites with increasing temperature and therefore becomes superparamagnetic. On the other hand, the FC curve tends to attain saturation below T_B signifying spin-glass like behavior in these nanoparticles. Apparently, the nanoparticles are ferrimagnetic dressed with spin-glass behavior below T_B and superparamagnetic above T_B . This, however, is consistent with the corresponding $M-H$ curves taken at 300 K and 10 K (see Fig. 6). To further confirm the superparamagnetic nature of these nanoparticles above T_B , we calculated the critical size (D) for a spherical nanoparticle to enter the superparamagnetic regime from above using [43]

$$D = 2 \left(\frac{6 k_B T_B}{K} \right)^{1/3} \quad (6)$$

where K is the magnetic anisotropy energy. For the $x = 0.75$ ferrite nanoparticles and using $T_B = 150$ K and $K = K_1 = 0.6 \times 10^6$ erg/cm³. The obtained value of $4D$ is ~ 11.8 nm, which is typically the same value obtained from XRD analysis (see Table 2), indicating that the prepared $x = 0.75$ ferrite nanoparticles are indeed superparamagnetic above T_B .

The $x = 1$ ferrite nanoparticles are superparamagnetic by default at room temperature. This is consistent with the corresponding room temperature $M-H$ curve that has almost zero coercivity and zero remanence. For $T < T_B \approx 100$ K, the nanoparticles show weak ferrimagnetic behavior with small coercivity as evidenced from the corresponding $M-H$ curve at 10 K (see Fig. 6). It is well known that bulk ZnFe_2O_4 ferrite is antiferromagnetic material below Neel's temperature ($T_N \approx 9$ K) and is paramagnetic above it. However, when particle size reduces to a certain range, it shows ferrimagnetic/superparamagnetic behavior which is evident from the corresponding $M-H$ magnetization curve at 10 K and the low temperature portion of the ZFC magnetization curve shown in Fig. 8. The weak variation in the FC curve below T_B is also an indication of the presence of spin-glass like behavior due to dipole-dipole interactions between the ferrite nanoparticles. For pure zinc ferrite nanoparticles ($x = 1$), the measured value of ($T_B \approx 100$ K) is almost twice that reported in [32] and four times bigger than that reported in [44]. Such discrepancy in the measured values of T_B for zinc ferrite is due to that the blocking temperature is sensitive to several factors such as synthesis method, annealing temperature, and size distribution.

4 Conclusion

$\text{Zn}_x\text{Co}_{1-x}\text{Fe}_2\text{O}_4$ ferrite nanoparticles with $x = 0, 0.25, 0.5, 0.75,$ and 1 were successfully synthesized via hydrothermal method with sizes smaller than 20 nm . XRD results showed that all the synthesized ferrites were cubic and single phase, and the increase in Zn concentration resulted in an increase in the lattice constant from 8.3706 \AA for $x = 0$ (CoFe_2O_4) to 8.4263 \AA for $x = 1$ (ZnFe_2O_4). The x-ray density was observed to increase with increasing Zn concentration from 5.31 g/cm^3 for $x = 0$ to 5.36 g/cm^3 for $x = 0.75$ and then decrease to 5.35 g/cm^3 for $x = 1$. The TEM measurements showed that the nanoparticles were monodisperse and spherical in shape. The FTIR results confirmed the formation of single phase spinel structure with two sub-lattices: tetrahedral and octahedral. The introduction of Zn ions into the parent cobalt ferrite caused remarkable changes in the magnetic properties. The room temperature $M-H$ magnetization measurements revealed that the ferrite nanoparticles were ferromagnetic for $x = 0$ and superparamagnetic for $x \geq 0.25$. At 10 K , all ferrite nanoparticles showed ferrimagnetic behavior that is weakened by Zn substitution. The saturation magnetization (M_s) was observed to decrease with increasing Zn concentration and the first anisotropy constant (K_1) was observed to decrease from $3.3 \times 10^6\text{ erg/cm}^3$ for $x = 0$ to $0.3 \times 10^6\text{ erg/cm}^3$ for $x = 1$. The ZFC-FC magnetization data revealed that both superparamagnetic and spin-glass like states may coexist together depending on amount of Zn concentration and temperature. We believe that understanding of origins and mechanisms of superparamagnetism and spin-glass behavior in these nanoparticles is expected to have a broad impact on utilizing them in several applications, mainly in data storage, magnetic recording, and biomedical applications.

Acknowledgements We gratefully acknowledge the financial support of the deanship of scientific research at the Hashemite University under Project Number: 5/2016. We also acknowledge the Nanotechnology Research Facility of Kuwait University under Project Number: GE01/07.

References

- R. Ashoori, Electrons in artificial atoms. *Nature* **379**(6564), 413 (1996)
- A. López-Ortega, E. Lottini, C.J. Fernandez, C. Sangregorio, Exploring the magnetic properties of cobalt-ferrite nanoparticles for the development of a rare-earth-free permanent magnet. *Chem. Mater.* **27**(11), 4048–4056 (2015)
- L. Zhao, H. Zhang, Y. Xing, S. Song, S. Yu, W. Shi, X. Guo, J. Yang, Y. Lei, F. Cao, Studies on the magnetism of cobalt ferrite nanocrystals synthesized by hydrothermal method. *J. Solid State Chem.* **181**(2), 245–252 (2008)
- Y. Zheng, L. Jia, F. Xu, G. Wang, X. Shi, H. Zhang, Microstructures and magnetic properties of low temperature sintering NiCuZn ferrite ceramics for microwave applications. *Ceram. Int.* **45**(17), 22163–22168 (2019)
- M. Amiri, M. Salavati-Niasari, A. Akbari, Magnetic nanocarriers: evolution of spinel ferrites for medical applications. *Adv. Colloid Interface Sci.* **265**, 29–44 (2019)
- T. Dippong, E.A. Levei, O. Cadar, I.G. Deac, L. Diamandescu, L. Barbu-Tudoran, Effect of nickel content on structural, morphological and magnetic properties of $\text{NiCo}_1-x\text{Fe}_2\text{O}_4/\text{SiO}_2$ nanocomposites. *J. Alloy. Compd.* **786**, 330–340 (2019)
- A. Goldman, *Modern Ferrite Technology* (Springer, Berlin, 2006)
- R. Raland, D. Saikia, C. Borgohain, J. Borah, Heating efficiency and correlation between the structural and magnetic properties of oleic acid coated MnFe_2O_4 nanoparticles for magnetic hyperthermia application. *J. Phys. D Appl. Phys.* **50**(32), 325004 (2017)
- R. Valenzuela, *Magnetic Ceramics*, vol. 4 (Cambridge University Press, Cambridge, 2005)
- X. Meng, H. Li, J. Chen, L. Mei, K. Wang, X. Li, Mössbauer study of cobalt ferrite nanocrystals substituted with rare-earth Y^{3+} ions. *J. Magn. Magn. Mater.* **321**(9), 1155–1158 (2009)
- T. Dippong, F. Goga, E.-A. Levei, O. Cadar, Influence of zinc substitution with cobalt on thermal behaviour, structure and morphology of zinc ferrite embedded in silica matrix. *J. Solid State Chem.* **275**, 159–166 (2019)
- M.S. Darwish, H. Kim, H. Lee, C. Ryu, J.Y. Lee, J. Yoon, Synthesis of magnetic ferrite nanoparticles with high hyperthermia performance via a controlled co-precipitation method. *Nanomaterials* **9**(8), 1176 (2019)
- A. Tawfik, I. Hamada, O. Hemeda, Effect of laser irradiation on the structure and electromechanical properties of Co-Zn ferrite. *J. Magn. Magn. Mater.* **250**, 77–82 (2002)
- G. Duong, N. Hanh, D. Linh, R. Groessinger, P. Weinberger, E. Schafner, M. Zehetbauer, Monodispersed nanocrystalline $\text{Co}_{1-x}\text{Zn}_x\text{Fe}_2\text{O}_4$ particles by forced hydrolysis: synthesis and characterization. *J. Magn. Magn. Mater.* **311**(1), 46–50 (2007)
- U. Naresh, R.J. Kumar, K.C.B. Naidu, Hydrothermal synthesis of barium copper ferrite nanoparticles: nanofiber formation, optical, and magnetic properties. *Mater. Chem. Phys.* **236**, 121807 (2019)
- G. Maity, P. Maji, S. Sain, S. Das, T. Kar, S. Pradhan, Microstructure, optical and electrical characterizations of nanocrystalline ZnAl_2O_4 spinel synthesized by mechanical alloying: effect of sintering on microstructure and properties. *Physica E* **108**, 411–420 (2019)
- D.S. Mathew, R.-S. Juang, An overview of the structure and magnetism of spinel ferrite nanoparticles and their synthesis in microemulsions. *Chem. Eng. J.* **129**(1–3), 51–65 (2007)
- C. Chinnasamy, B. Jeyadevan, K. Shinoda, K. Tohji, D. Djayaprawira, M. Takahashi, R.J. Joseyphus, A. Narayanasamy, Unusually high coercivity and critical single-domain size of nearly monodispersed CoFe_2O_4 nanoparticles. *Appl. Phys. Lett.* **83**(14), 2862–2864 (2003)
- T. Dippong, E.A. Levei, I.G. Deac, E. Neag, O. Cadar, Influence of Cu^{2+} , Ni^{2+} , and Zn^{2+} ions doping on the structure, morphology, and magnetic properties of co-ferrite embedded in SiO_2 matrix obtained by an innovative sol-gel route. *Nanomaterials* **10**(3), 580 (2020)
- H. Jalili, B. Aslibeiki, A.G. Varzaneh, V.A. Chernenko, The effect of magneto-crystalline anisotropy on the properties of hard and soft magnetic ferrite nanoparticles. *Beilstein J. Nanotechnol.* **10**(1), 1348–1359 (2019)
- S. Amiri, H. Shokrollahi, The role of cobalt ferrite magnetic nanoparticles in medical science. *Mater. Sci. Eng., C* **33**(1), 1–8 (2013)
- M. Şincal, D. Gâng, D. Bica, L. Vékás, The antitumor effect of locoregional magnetic cobalt ferrite in dog mammary adenocarcinoma. *J. Magn. Magn. Mater.* **225**(1–2), 235–240 (2001)

23. A.L. Tiano, G.C. Papaefthymiou, C.S. Lewis, J. Han, C. Zhang, Q. Li, C. Shi, A.M. Abeykoon, S.J. Billinge, E. Stach et al., Correlating size and composition-dependent effects with magnetic, mossbauer, and pair distribution function measurements in a family of catalytically active ferrite nanoparticles. *Chem. Mater.* **27**(10), 3572–3592 (2015)
24. R.A. Young, *The Rietveld Method*, vol. 5 (International Union of Crystallography, Chester, 1993)
25. K.E. Sickafus, R. Hughes, *Spinel Compounds: Structure and Property Relations* (American Ceramic Society, Westerville, 1999)
26. L. Kumar, P. Kumar, A. Narayan, M. Kar, Rietveld analysis of xrd patterns of different sizes of nanocrystalline cobalt ferrite. *Int. Nano Lett.* **3**(1), 8 (2013)
27. R. Bujakiewicz-Korońska, Ł. Hetmańczyk, B. Garbarz-Głos, A. Budziak, A. Kalvane, K. Bormanis, K. Druzbicki, Low temperature measurements by infrared spectroscopy in cofe₂o₄ ceramic. *Open Phys.* **10**(5), 1137–1143 (2012)
28. J. Gomes, M. Sousa, F. Tourinho, J. Mestnik-Filho, R. Itri, J. Depeyrot, Rietveld structure refinement of the cation distribution in ferrite fine particles studied by x-ray powder diffraction. *J. Magn. Magn. Mater.* **289**, 184–187 (2005)
29. R.D. Shannon, Revised effective ionic radii and systematic studies of interatomic distances in halides and chalcogenides. *Acta Crystallogr. Sect. A: Cryst. Phys., Diffr., Theor. General Crystallogr.* **32**(5), 751–767 (1976)
30. B. Toksha, S.E. Shirsath, S. Patange, K. Jadhav, Structural investigations and magnetic properties of cobalt ferrite nanoparticles prepared by sol-gel auto combustion method. *Solid State Commun.* **147**(11–12), 479–483 (2008)
31. D.S. Nikam, S.V. Jadhav, V.M. Khot, R. Bohara, C.K. Hong, S.S. Mali, S. Pawar, Cation distribution, structural, morphological and magnetic properties of co_{1-x}zn_xfe₂o₄ (x= 0–1) nanoparticles. *RSC Adv.* **5**(3), 2338–2345 (2015)
32. K. Praveena, K. Sadhana, Ferromagnetic properties of zn substituted spinel ferrites for high frequency applications. *Int. J. Sci. Res. Publ.* **5**(4), 1–21 (2015)
33. S.-T. Xu, Y.-Q. Ma, Y.-F. Xu, X. Sun, B.-Q. Geng, G.-H. Zheng, Z.-X. Dai, Pure dipolar-interacted cofe₂o₄ nanoparticles and their magnetic properties. *Mater. Res. Bull.* **62**, 142–147 (2015)
34. M. Chithra, C. Anumol, B. Sahu, S.C. Sahoo, Structural and magnetic properties of znxco_{1-x}fe₂o₄ nanoparticles: nonsaturation of magnetization. *J. Magn. Magn. Mater.* **424**, 174–184 (2017)
35. L. Kumar, M. Kar, Effect of annealing temperature and preparation condition on magnetic anisotropy in nanocrystalline cobalt ferrite. *IEEE Trans. Magn.* **47**(10), 3645–3648 (2011)
36. K. Maaz, A. Mumtaz, S. Hasanain, A. Ceylan, Synthesis and magnetic properties of cobalt ferrite (cofe₂o₄) nanoparticles prepared by wet chemical route. *J. Magn. Magn. Mater.* **308**(2), 289–295 (2007)
37. C. Iacovita, A. Florea, L. Scorus, E. Pall, R. Dudric, A.I. Moldovan, R. Stiuflu, R. Tetean, C.M. Lucaciu, Hyperthermia, cytotoxicity, and cellular uptake properties of manganese and zinc ferrite magnetic nanoparticles synthesized by a polyol-mediated process. *Nanomaterials* **9**(10), 1489 (2019)
38. R. Topkaya, A. Baykal, A. Demir, Yafet-Kittel-type magnetic order in zn-substituted cobalt ferrite nanoparticles with uniaxial anisotropy. *J. Nanopart. Res.* **15**(1), 1359 (2013)
39. G. Muscas, S. Jovanović, M. Vukomanović, M. Spreitzer, D. Peddis, Zn-doped cobalt ferrite: tuning the interactions by chemical composition. *J. Alloy. Compd.* **796**, 203–209 (2019)
40. A. Nairan, M. Khan, U. Khan, M. Iqbal, S. Riaz, S. Naseem, Temperature-dependent magnetic response of antiferromagnetic doping in cobalt ferrite nanostructures. *Nanomaterials* **6**(4), 73 (2016)
41. E. Del Barco, J. Asenjo, X. Zhang, R. Pieczynski, A. Julia, J. Tejada, R. Ziolo, D. Fiorani, A. Testa, Free rotation of magnetic nanoparticles in a solid matrix. *Chem. Mater.* **13**(5), 1487–1490 (2001)
42. K. Nadeem, H. Krenn, T. Traußnig, R. Würschum, D. Szabó, I. Letofsky-Papst, Effect of dipolar and exchange interactions on magnetic blocking of maghemite nanoparticles. *J. Magn. Magn. Mater.* **323**(15), 1998–2004 (2011)
43. A.G. Kolhatkar, A.C. Jamison, D. Litvinov, R.C. Willson, T.R. Lee, Tuning the magnetic properties of nanoparticles. *Int. J. Mol. Sci.* **14**(8), 15977–16009 (2013)
44. W. Mohamed, M. Alzaid, M.S.M. Abdelbaky, Z. Amghouz, S. García-Granda, A.M. Abu-Dief, Impact of Co²⁺ substitution on microstructure and magnetic properties of coxzn_{1-x}fe₂o₄ nanoparticles. *Nanomaterials* **9**(11), 1602 (2019)

Publisher's Note Springer Nature remains neutral with regard to jurisdictional claims in published maps and institutional affiliations.